
PROCESS-TENSOR TOMOGRAPHY OF SGD: MEASURING NON-MARKOVIAN MEMORY VIA BACK-FLOW OF DISTINGUISHABILITY *

Vasileios Sevetlidis*

Athena RC

University Campus Kimmeria
Xanthi, GR67100, Greece
vasiseve@athenarc.gr

George Pavlidis

Athena RC

University Campus Kimmeria
Xanthi, GR67100, Greece
gpavlid@athenarc.gr

ABSTRACT

This work proposes neural training as a *process tensor*: a multi-time map that takes a sequence of controllable instruments (batch choices, augmentations, optimizer micro-steps) and returns an observable of the trained model. Building on this operational lens, we introduce a simple, model-agnostic witness of training memory based on *back-flow of distinguishability*. In a controlled two-step protocol, we compare outcome distributions after one intervention versus two; the increase $\Delta_{\text{BF}} = D_2 - D_1 > 0$ (with $D \in \{\text{TV, JS, H}\}$ measured on softmax predictions over a fixed probe set) certifies non-Markovianity. We observe consistent positive back-flow with tight bootstrap confidence intervals, amplification under higher momentum, larger batch overlap, and more micro-steps, and collapse under a *causal break* (resetting optimizer state), directly attributing the effect to optimizer/data-state memory. The witness is robust across TV/JS/Hellinger, inexpensive to compute, and requires no architectural changes. We position this as a *measurement* contribution: a principled diagnostic and empirical evidence that practical SGD deviates from the Markov idealization. An exploratory case study illustrates how the micro-level signal can inform curriculum orderings. “Data order matters” turns into a testable operator with confidence bounds, our framework offers a common stage to compare optimizers, curricula, and schedules through their induced training memory.

Keywords training dynamics, process tensor, non-Markovianity, stochastic gradient descent, back-flow, distinguishability, momentum, causal break, curriculum learning, probe set

1 INTRODUCTION

Modern training pipelines make—and often quietly rely on—simplifying assumptions about how updates compose over time. In particular, theoretical analyses frequently model training as (approximately) Markovian once the algorithm’s internal buffers are included in the state: a future iterate is conditionally independent of earlier choices given current parameters and optimizer state. This idealization keeps proofs tractable, but it leaves practitioners without a direct, operational way to *measure* whether a real training run is memoryless or history-dependent. Empirical analyses of

* Citation (to appear in): Vasileios Sevetlidis, and George Pavlidis. Process-Tensor Tomography of SGD: Measuring Non-Markovian Memory via Back-Flow of Distinguishability. Proceedings of The 29th International Conference on Artificial Intelligence and Statistics, in Proceedings of Machine Learning Research. 2026

reshuffling and curricula confirm that order matters, and optimizer designs intentionally carry history, yet there is no simple diagnostic that a practitioner can run to falsify a “memoryless training” hypothesis [1, 2, 3, 4, 5]. A concrete pain point is schedule design (data order, augmentations, and optimizer knobs): many heuristics work, yet we lack a principled diagnostic to tell when past choices still influence today’s outcomes [6, 7].

We build on operational notions of non-Markovianity developed in open quantum systems. There, increases in distinguishability between states (“information back-flow”) certify memory effects [8, 9]. The *process tensor* formalism elevates this to a full multi-time description: dynamics are maps from sequences of controllable *instruments* to outcome distributions, with a sharp *operational Markov condition* and the notion of a *causal break* [10, 11]. Comprehensive reviews and tomographic schemes further consolidate this perspective [12, 13]. In our classical setting, we treat training as a process tensor: a multi-time map from chosen instruments (batch selection, augmentation, optimizer micro-step) to observables (predictions on a probe set). We quantify distinguishability using TV/JS/Hellinger metrics on model outputs, and we implement a causal break by *resetting optimizer state*. Adapting the standard witness from open-systems theory, we test for *back-flow of distinguishability*: run two one-step histories that differ only in the first intervention A vs. A' , then apply a common second intervention B . If the distance between resulting prediction distributions increases after B , we certify memory (non-Markovianity). This transposes the trace-distance back-flow criterion and process-tensor framework into the context of SGD.

Contributions.

1. **Operational witness for SGD memory.** We introduce a two-step A/B protocol and a *back-flow* statistic computed on predictive distributions (TV/JS/Hellinger). The method is measurement-only and model-agnostic.
2. **Mechanism test via causal break.** We instantiate a “break” (reset optimizer state) before B . If optimizer buffers mediate memory, Δ should collapse—a direct, falsifiable mechanism check [11].
3. **Empirical process-tomography of training.** On CIFAR-10 and Imagenette across multiple architectures and three divergences, we measure Δ under controlled regimes (standard, resonant, orthogonal, negative) and report seed-robust CIs.
4. **Ablations that map the control parameters.** We chart how Δ scales with momentum, batch overlap, and step depth; and we quantify the collapse under causal break.

The structure of this work is as follows: background and related work is presented in §2; §3 formalizes the process-tensor view and the back-flow witness; §4 details the A/B protocol and the causal-break mechanism test; §5 reports measurements and ablations. Code, logs, and plotting scripts accompany the paper for full reproducibility.

2 RELATED WORK

Analyses of stochastic optimization often treat updates as (time-homogeneous) Markov dynamics once one augments the state with algorithmic buffers and assumes i.i.d. sampling. This viewpoint underpins tutorials and SDE-based models of SGD: it enables mixing/ergodicity arguments and stationary-distribution pictures near minima [6, 7]. Sampling *without* replacement (random reshuffling) couples consecutive steps through the epoch permutation and changes both analysis and practice; multiple works prove or quantify RR’s advantages and make its temporal dependence explicit. These effects can be re-cast as Markov only by further augmenting the state (e.g., with a permutation pointer), underscoring that order is a first-class control knob in modern training [1, 14, 2]. Momentum and adaptive methods explicitly accumulate history. Classic and modern accounts (heavy-ball, [15]; [3]; (**author?**) [4]’s Distill note) document their empirical and dynamical impact; stochastic modified-equation analyses encode them as SDEs in an *enlarged* state. Our *causal break* experiment operationalizes this intuition: if buffers mediate history, resetting them should null out back-flow—which is exactly what we observe [16, 17].

A separate line treats the *data source* as Markov and tracks the role of mixing time in SGD’s convergence—formally moving dependence from the algorithm to the sampler. This is adjacent to, but distinct from, our aim: we test for history-dependence in the *training process* as exposed by output distributions under controlled interventions [5, 18, 19]. Empirical work finds that gradient noise during deep learning is heavy-tailed and anisotropic, challenging Gaussian, white-noise assumptions common in SDE models. While not phrased in “Markov vs. non-Markov” terms, these observations motivate measurement-first diagnostics that do not hinge on specific noise models [20, 21]. Several diagnostics quantify how predictions or representations change across training. LOOD-type measures track output changes induced by adding/removing examples (aimed at privacy/memorization) [22, 23, 24, 25, 26, 27], while representation-similarity metrics (e.g., CKA) probe internal drift [28]. Recent work questions their reliability and sensitivity [29]. In contrast, our witness is *non-parametric*, *intervention-defined*, and explicitly tied to an operational Markov condition.

3 Methodology

We formalize a short segment of training as a multi-time stochastic process that maps *instruments*—controllable, randomized interventions—to a distribution over *observables* on a fixed probe set. The key object is a classical *process tensor* (comb) acting at two times; our operational witness of memory is a *back-flow of distinguishability* between two one-step histories under a fixed second intervention. We prove that a positive back-flow contradicts an *operational Markov* condition at the observable, and we show that a *causal break* (resetting optimizer buffers) restores that condition under a mild sufficiency hypothesis, predicting the collapse of our witness.

3.1 State spaces, instruments, and kernels

Let $(\mathcal{S}, \Sigma_{\mathcal{S}})$ be a standard Borel space for the *latent algorithmic state* (parameters and any optimizer buffers), and $(\mathcal{O}, \Sigma_{\mathcal{O}})$ an observable space (per-example class probabilities on a fixed probe set). A *stochastic kernel* $K : \mathcal{A} \times \Sigma_{\mathcal{B}} \rightarrow [0, 1]$ maps each $a \in \mathcal{A}$ to a probability measure on $(\mathcal{B}, \Sigma_{\mathcal{B}})$ and is measurable in a .

An *instrument* I specifies: (i) a mini-batch index set, (ii) a data-augmentation kernel, and (iii) optimizer micro-parameters used for k micro-steps. Executing I induces a latent kernel $\mathcal{K}_I : \mathcal{S} \rightsquigarrow \mathcal{S}$ (the random update over k micro-steps). Given two successive instruments I_0, I_1 and an initial prior $\pi_0 \in \mathcal{P}(\mathcal{S})$, the latent two-time law is

$$\pi_2^{(I_0, I_1)}(ds_2) = \int_{\mathcal{S}} \left[\int_{\mathcal{S}} \mathcal{K}_{I_1}(s_1, ds_2) \mathcal{K}_{I_0}(s_0, ds_1) \right] \pi_0(ds_0). \quad (1)$$

The *observation channel* $\mathcal{O} : \mathcal{S} \rightsquigarrow \mathcal{O}$ pushes latent state to predictions on the probe. The observable one- and two-time laws are then

$$\Phi_1^{(I_0)}(do) = \int_{\mathcal{S}} \mathcal{O}(s_1, do) \pi_1^{(I_0)}(ds_1), \quad (2)$$

$$\Phi_2^{(I_0, I_1)}(do) = \int_{\mathcal{S}} \mathcal{O}(s_2, do) \pi_2^{(I_0, I_1)}(ds_2), \quad (3)$$

where $\pi_1^{(I_0)} = \pi_0 \mathcal{K}_{I_0}$ and composition is the usual *link product* of kernels: $(K_2 \star K_1)(a, dc) := \int K_2(b, dc) K_1(a, db)$.

Collecting all two-time statistics defines a multilinear map

$$\mathsf{T}_{2:0} : \mathcal{I}_0 \times \mathcal{I}_1 \rightarrow \mathcal{P}(\mathcal{O}), \quad (I_0, I_1) \mapsto \Phi_2^{(I_0, I_1)},$$

where \mathcal{I}_t is a convex set of admissible (randomized) instrument kernels. In the classical setting, complete positivity reduces to *stochasticity* and *non-negativity* under linking with any admissible post-processing on observables.

3.2 Operational Markov condition at the observable

Definition 1. *Operational Markov condition (OMC) at the observable.* Fix a second-step instrument B . We say that the two-time process is operationally Markov at the observable for B if there exists a stochastic map $\Lambda_B : \mathcal{P}(\mathcal{O}) \rightarrow \mathcal{P}(\mathcal{O})$ such that for every first-step instrument I ,

$$\Phi_2^{(I, B)} = \Lambda_B[\Phi_1^{(I)}]. \quad (4)$$

Proposition 3.1 (Proposition 3.1). *If the two-time process is operationally Markov at the observable for B , then for any contractive divergence D , the back-flow of distinguishability satisfies $\Delta^{(I, B)} \leq 0$ for all I .*

Intuitively, once the observed mid-time law Φ_1 is fixed, B acts by the *same channel* on it, independent of how Φ_1 was prepared. Condition (4) is strictly weaker than assuming latent Markov dynamics in $(\theta, \text{buffers})$: it only constrains the *measured map*.

3.3 A back-flow witness of operational memory

Choose two first-step instruments A, A' (same indices, different augmentation) and fix B . Let D be a divergence on $\mathcal{P}(\mathcal{O})$ that obeys data processing (see §3.6). Define

$$D_1 := D(\Phi_1^{(A)}, \Phi_1^{(A')}), \quad (5)$$

$$D_2 := D(\Phi_2^{(A, B)}, \Phi_2^{(A', B)}), \quad (6)$$

$$\Delta_{\text{BF}} := D_2 - D_1. \quad (7)$$

Proposition 3.2 (No back-flow under OMC). *If (4) holds and D satisfies data processing, then $\Delta_{\text{BF}} \leq 0$.*

Thus, *positive* back-flow ($\Delta_{\text{BF}} > 0$) *falsifies* (4) and witnesses operational memory at the two-step scale. Mechanistically this can arise because (i) history is *carried* across the step by unobserved buffers that modulate the action of B , or (ii) the observable is *insufficient* for how B acts: two distinct latent preparations that agree on Φ_1 evolve differently under B .

3.4 Causal break and a sufficient condition for restoring OMC

A *causal break* before B is a kernel $\mathcal{B} : \mathcal{S} \rightsquigarrow \mathcal{S}$ that erases a memory channel we intend to cut. In our setting, it resets optimizer buffers while keeping parameters fixed: if $s = (\theta, v)$, then $\mathcal{B}(s, d\theta' dv') = \delta_\theta(d\theta') \delta_0(dv')$. Let $\tilde{\mathcal{K}}_B := \mathcal{K}_B \star \mathcal{B}$ be the post-break latent kernel.

We give a mild, checkable condition under which the break implies (4).

Definition 2 (Observable sufficiency for B). *Let $\mathcal{Q} \subseteq \mathcal{P}(\mathcal{S})$ be the set of mid-time latent laws reachable after the first step. The observation channel \mathcal{O} is sufficient for B on \mathcal{Q} if for any $\pi_1, \pi'_1 \in \mathcal{Q}$ with equal observables $\pi_1 \mathcal{O}^{-1} = \pi'_1 \mathcal{O}^{-1}$, we also have $\pi_1 \tilde{\mathcal{K}}_B \mathcal{O}^{-1} = \pi'_1 \tilde{\mathcal{K}}_B \mathcal{O}^{-1}$.*

Theorem 3.1. (*Break \Rightarrow observable channel under sufficiency.*) *If a causal break \mathcal{B} is applied and \mathcal{O} is sufficient for B on \mathcal{Q} , then there exists a stochastic map Λ_B on $\mathcal{P}(\mathcal{O})$ such that for all first-step instruments I , $\Phi_2^{(I, B)} = \Lambda_B[\Phi_1^{(I)}]$. Consequently, $\Delta_{\text{BF}} \leq 0$ for any contractive divergence D .*

A sufficient way to ensure Def. 2 is a *Markov factorization* through the observable: there exists a lifting kernel $R : \mathcal{O} \rightsquigarrow \mathcal{S}$ (a right-inverse of \mathcal{O} on \mathcal{Q}) such that $\tilde{\mathcal{K}}_B = \tilde{\mathcal{K}}_B \star R \star \mathcal{O}$ on \mathcal{Q} . Then $\Lambda_B = \mathcal{O} \star \tilde{\mathcal{K}}_B \star R$ is explicit.

3.5 Perturbative scaling predictions

A first-order linearization explains the observed trends with momentum, batch overlap, and micro-step depth. Write the k -step update under instrument I as $U_I(\theta) \approx \theta - \eta \sum_{t=0}^{k-1} \hat{g}_I(\theta, t)$, where \hat{g} incorporates momentum μ via $\hat{g}_I(\cdot, t) \approx (1 - \mu) \sum_{i=0}^t \mu^i g_I(\cdot)$. For the two histories A, A' ,

$$\theta_1^{(A)} - \theta_1^{(A')} \approx -\eta \sum_{t=0}^{k-1} (\hat{g}_A - \hat{g}_{A'})(\theta_0, t),$$

and after applying B once more,

$$\begin{aligned} \theta_2^{(A, B)} - \theta_2^{(A', B)} &\approx \left(I - \eta k H_B(\theta_0) \right) (\theta_1^{(A)} - \theta_1^{(A')}) \\ &\quad + \eta k \Xi_{AB}. \end{aligned}$$

where H_B is a (preconditioned) Jacobian/Hessian of the B -gradient and Ξ_{AB} collects curvature–noise cross-terms. Two corollaries match our measurements: (i) **Momentum amplification**: $\|\theta_1^{(A)} - \theta_1^{(A')}\|$ scales like $(1 - \mu^k)/(1 - \mu)$, so $D_2 - D_1$ increases with μ . (ii) **Resonance via overlap**: when B reuses samples from A (overlap ρ), H_B and Ξ_{AB} correlate with $g_A - g_{A'}$, enlarging $D_2 - D_1$; disjoint B damps it. A causal break zeros momentum at the second step, removing the μ -dependent amplification and driving $\Delta_{\text{BF}} \rightarrow 0$ up to $\mathcal{O}(\eta^2)$.

3.6 Divergences and contractivity

We operate on per-example predictive distributions over the probe set and aggregate by averaging the per-example divergence.² We require boundedness in $[0, 1]$, sensitivity to multi-class changes, and data processing: *total variation* $\text{TV}(p, q) = \frac{1}{2} \|p - q\|_1$, and *Hellinger* $\text{Hell}(p, q) = \frac{1}{2} \|\sqrt{p} - \sqrt{q}\|_2$ are f -divergences and thus contractive under stochastic maps; *Jensen–Shannon* $\text{JS}(p, q) = \frac{1}{2} \text{KL}(p\|m) + \frac{1}{2} \text{KL}(q\|m)$, $m = \frac{1}{2}(p + q)$ is a symmetrized mixture of KL and inherits the same property. Proposition 3.2 therefore applies to all three.

²Formally, if $x \in \mathcal{P}$ ranges over probe inputs and P_x, Q_x are the class-probability vectors under two histories, we use $\bar{D}(P, Q) := \frac{1}{|\mathcal{P}|} \sum_{x \in \mathcal{P}} D(P_x, Q_x)$. If D obeys data processing pointwise, so does \bar{D} .

3.7 Inference at the observable level

Each run produces random variables $D_1, D_2 \in [0, 1]$ and $\Delta_{\text{BF}} \in [-1, 1]$. We treat the *operational Markov* inequality as the null $H_0 : \mathbb{E}[\Delta_{\text{BF}}] \leq 0$. We report nonparametric bootstrap CIs for the mean and perform TOST (*two one-sided tests*) against a small equivalence margin ε to declare practical nullity. A lower confidence bound strictly above 0 rejects H_0 and certifies operational non-Markovianity for the specified instruments and observable; collapse toward 0 after a causal break supports the mechanism diagnosis in §3.4.

3.8 What a positive back-flow *means* (and what it does not)

A strictly positive Δ_{BF} says there is *no* single channel Λ_B that maps *the measured* one-step laws to the two-step laws for the fixed B . It *does not* claim the augmented latent dynamics (θ , buffers) are non-Markov; rather, it pinpoints an observable-level failure of (4). Our causal-break experiments remove optimizer memory as a carrier and are consistent with the picture that, at the two-step scale we probe, buffers mediate the observed dependence.

4 EXPERIMENTAL PROCEDURE

Table 1: Micro-step regimes.

Regime	k	LR	mom	aug_A	$\text{aug}_{A'}$	aug_B	overlap / classes
standard	3	0.02	0.90	weak	color	weak	0.5 / True
resonant strong	6	0.03	0.99	color	blur	weak	1.0 / True
resonant mid	6	0.03	0.95	color	blur	weak	0.75 / True
orthogonal	6	0.03	0.99	color	blur	blur	0.0 / False
negative (ctrl)	1	0.005	0.00	none	none	none	0.0 / False

We instantiate the two-step $A \rightarrow B$ protocol from §3 across datasets, model families, and micro-step “regimes,” and measure the observable-level back-flow $\Delta_{\text{BF}} = D_2 - D_1$ using TV (primary) and JS/H (secondary). The only conceptual manipulation relative to §3 is the *causal break*: either we carry the optimizer buffers from A into B (*no break*) or we re-initialize the optimizer immediately before B (*break*), holding hyperparameters fixed. Everything else below specifies what each symbol means in practice.

We evaluate on CIFAR-100 and Imagenette. Inputs are resized to 32×32 (RGB). For Imagenette we use the official validation split as held-out data. Backbones: SmallCNN, ResNet-18 (CIFAR stem), VGG-11, MobileNetV2, and a ViT-B/16 configured for 32×32 (2×2 patches). The final linear heads match the dataset’s number of classes.

Unless otherwise stated, we use the *early* stage: SGD (LR 0.1, momentum 0.9, weight decay 5×10^{-4}), cosine schedule over 3 epochs with weak CPU-side augmentation (random crop 32 with pad 4 and horizontal flip). We also retain `init` (random) and `late` (20 epochs) for sensitivity checks. A GPU snapshot of the base parameters is cached to enable fast, in-place resets between micro-experiments.

4.1 Micro-step protocol (A then B)

A single *micro-experiment* starts from the cached base parameters, applies k SGD steps on a mini-batch stream from A , then k steps from B . Unless otherwise specified: batch size 256, per-step weight decay 10^{-4} , gradient clip at 1.0, channels-last memory layout, and *AMP disabled* (the code path supports it but we keep it off in the sweep). BatchNorm running statistics are frozen during micro-steps.

We implement GPU-native transforms: *weak* = random crop (32, reflect pad 4) + horizontal flip ($p=0.5$); *color* = weak + color jitter (brightness/contrast/saturation 0.4) + random grayscale ($p=0.2$); *blur* = weak + depthwise Gaussian blur (kernel 3, $\sigma \sim \mathcal{U}[0.1, 2.0]$); and *none* = identity.

For each repeat we draw I_A uniformly without replacement (size 256) from cached training tensors. We draw I_B to achieve a prescribed overlap with I_A , $|I_A \cap I_B| \approx \lfloor \text{overlap} \times 256 \rfloor$, and optionally match the *class histogram* of I_A (`same_classes=True`), otherwise draw from the complement. This gives fine control of content resonance between A and B .

Fixing (I_A, I_B) and augmentations $(\text{aug}_A, \text{aug}_{A'}, \text{aug}_B)$,

$$\theta_A \xrightarrow{B} \theta_{AB} \quad \text{vs.} \quad \theta_{A'} \xrightarrow{B} \theta_{A'B},$$

where A and A' differ only by augmentation on the *same* I_A . We compute D_1 and D_2 on a held-out probe and report Δ_{BF} .

In the *no break* condition B uses the optimizer state carried from A (e.g., momentum buffers). In the *break* condition we re-initialize the optimizer immediately before B (same LR/momentum), which implements the observable-level causal break discussed in §3.4.

4.2 Probe set and observable distances

For each (dataset, model) we fix a probe of $N=2000$ held-out examples (Imagenette: validation; CIFAR-100: test). Given parameters θ , we compute softmax probabilities on the probe to form $P(\theta) \in \mathbb{R}^{N \times C}$. As in §3.6, we aggregate per-example divergences to obtain D_1 (after the first step) and D_2 (after the second), and report Δ_{BF} ; TV is our primary metric, with JS and H for robustness checks.

We sweep four substantive regimes plus a negative control, each specifying (k,LR, momentum, aug_A , $\text{aug}_{A'}$, aug_B , overlap, same_classes), as shown in Table 1.

To contextualize Δ_{BF} , we log four diagnostics once per seed and regime (to bound cost):

1. **Non-commutativity** ($AB \neq BA$): for $k \in \{1, \dots, 6\}$ we compare endpoints $\theta_{AB}^{(k)}$ vs. $\theta_{BA}^{(k)}$ via $\text{TV}(P(\theta_{AB}^{(k)}), P(\theta_{BA}^{(k)}))$ on a 512-example probe subset.
2. **Momentum alignment (no break only):** $\cos(\nabla_{\theta} \ell_B, m)$ between the B -gradient and the optimizer’s momentum buffer just before the first B step.
3. **Penultimate feature drift:** linear CKA on the input to the final linear layer for (A, A') and $(AB, A'B)$ using the 512-example probe subset.
4. **Function-space trajectory:** PCA of $\{P(\theta_A), P(\theta_{AB}), P(\theta_{A'}), P(\theta_{A'B})\}$; we plot branch centroids ($A \rightarrow AB$ vs. $A' \rightarrow A'B$).

4.3 Repeats, seeds, precision targets

For each (dataset, model, regime, break flag) and each seed $s \in \{0, 1, 2, 3, 4\}$, we run $R=128$ independent repeats (fresh (I_A, I_B) per repeat). To control runtime while keeping tight confidence intervals, after at least 64 repeats we check every 32 repeats whether the nominal half-width of the 95% CI for Δ_{BF} (normal approximation) is $\leq 2 \times 10^{-4}$ and stop early if so. We then aggregate per-configuration means with 2000-sample nonparametric bootstrap CIs (on per-repeat Δ_{BF}). For completeness we also perform TOST with equivalence margin $\varepsilon=10^{-3}$. All micro-experiments use SGD; gradients are clipped at 1.0; a NaN guard and a fallback LR scaling ($\times 0.5$ on retry) handle rare numerical issues. We freeze BN running stats during micro-steps, and run inference in channels-last format. The orchestration writes per-seed logs and a post-processing script emits a `summary` with mean Δ_{BF} and bootstrap CIs, alongside diagnostic figures³.

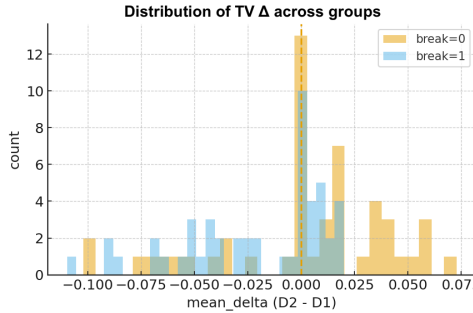


Figure 1: **Distribution of TV mean Δ_{BF} across all setups.** Histogram for *no break* and *break* conditions. The mass shifts toward attenuation under a causal break.

³These artifacts are the basis for §5

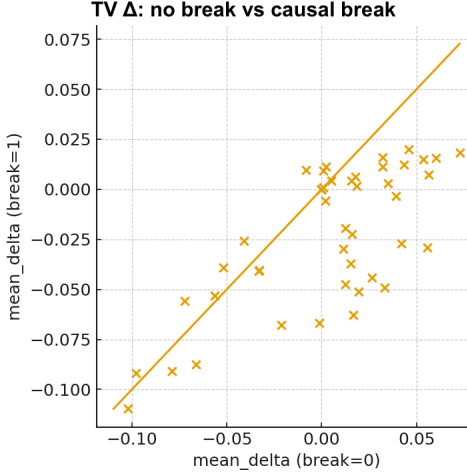


Figure 2: **TV mean effect: no break vs. break.** Each point is one $\{dataset, model, regime, base_stage\}$. Many points lie below the diagonal and 28% cross quadrants (sign flips), indicating that optimizer carryover causally drives amplification.

5 RESULTS

For each configuration we report the back-flow statistic $\Delta_{BF} := \mathbb{E}[D_2] - \mathbb{E}[D_1]$ on predictive distributions over a fixed probe set (TV primary; JS/H secondary). Intuitively, $\Delta_{BF} > 0$ means the second instrument *B amplifies* the functional discrepancy induced by *A* vs. *A'*, whereas $\Delta_{BF} < 0$ indicates *attenuation*. Unless stated otherwise, we show nonparametric bootstrap 95% CIs.

Across 50 unique $\{dataset, model, regime, base_stage\}$ setups and two optimizer conditions (*no break* vs. *causal break*), we obtain 100 TV groups. Significance is widespread effects with narrow CIs: with *no break*, 35 positive and 12 negative groups have CIs excluding 0 (only 3 non-significant); with a *causal break*, 22 positive and 25 negative are significant (again 3 non-significant). Every unique setup is significant in at least one condition and 44/50 are significant in *both*. Agreement across distances is strong: TV \wedge Hellinger is significant in 93/100 groups and TV \wedge JS in 80/100;⁴ see Fig. 1.

Introducing a *causal break* (reinitializing optimizer state before *B*) systematically changes both sign and magnitude of Δ_{BF} . A striking 14/50 (28%) of setups *flip sign* between conditions (Fig. 2), with large absolute changes concentrated in high-momentum, high-overlap regimes (Table 2)⁵. Thus, **optimizer carryover is causal**: the break flips signs in 28% of setups

Table 2: **Representative cases across both datasets (TV).** Rows 1–8 showcase sign flips; bottom rows give a strong attenuation baseline per dataset.

Dataset	Model	Regime	Stage	Δ_{no}	Δ_{br}	$\Delta_{br} - \Delta_{no}$
CIFAR-100	ViT-B/16	resonant_strong	early	0.0557	-0.0291	-0.0847
CIFAR-100	VGG-11	resonant_strong	early	0.0331	-0.0492	-0.0823
CIFAR-100	ViT-B/16	orthogonal	early	0.0168	-0.0629	-0.0797
CIFAR-100	ViT-B/16	resonant_mid	early	0.0266	-0.0442	-0.0708
CIFAR-100	MobileNetV2	orthogonal	early	0.0193	-0.0512	-0.0706
Imagenette	ViT-B/16	orthogonal	early	0.0393	-0.0032	-0.0426
Imagenette	ResNet-18	standard	early	0.0161	-0.0225	-0.0386
Imagenette	VGG-11	standard	early	0.0021	-0.0059	-0.0080
CIFAR-100	ResNet-18	resonant_mid	early	-0.1022	-0.1096	-0.0075
Imagenette	ResNet-18	resonant_mid	early	-0.0978	-0.0918	+0.0059

⁴TV-only significant and non-TV-only significant are rare: 0/100 and 2/100, respectively.

⁵Per-setup 95% CIs are reported in the appendix

Averaging TV across datasets and architectures reveals clear regime effects (Fig. 3). Without a break, standard, orthogonal, and resonant strong tend to *amplify* ($\Delta_{BF} > 0$); with a break they shift toward *attenuation* ($\Delta_{BF} < 0$). The negative control is near zero. Numerically (means across all dataset×model): standard +0.0127 → −0.00729, orthogonal +0.0103 → −0.0206, resonant strong +0.00734 → −0.0310, resonant mid −0.0177 → −0.0448, negative $\approx 6 \times 10^{-4}$ → 5×10^{-4} (medians $\approx 10^{-7}$). Hence, we observe **regime-level trends**: momentum and overlap amplify; break attenuates.

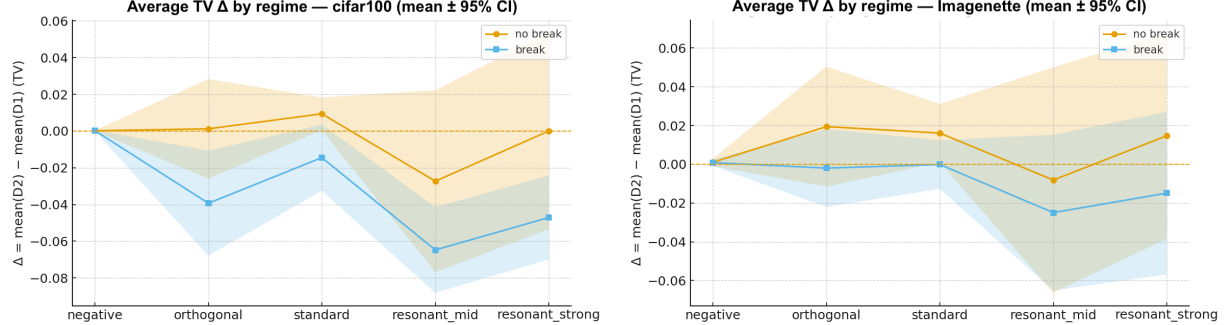


Figure 3: **Average TV effect by regime and optimizer condition.** Points are means across datasets and models; ribbons show bootstrap 95% CIs. High-momentum/high-overlap regimes amplify without a break and attenuate with a break.

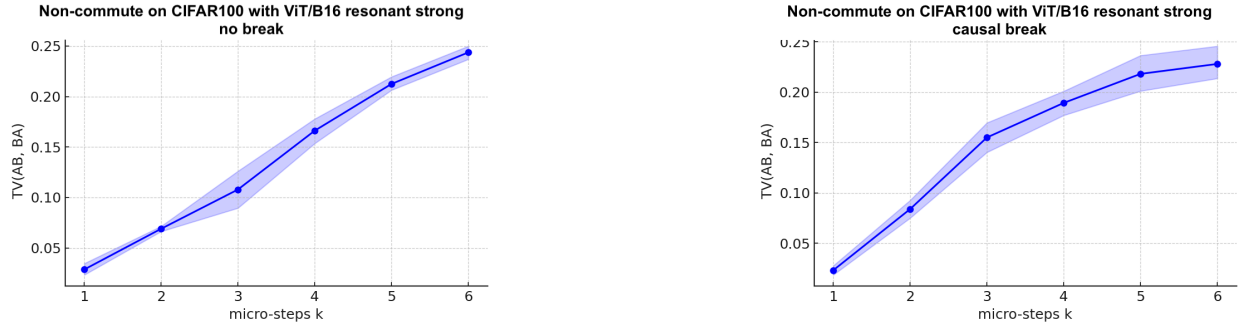


Figure 4: **Non-commute curves.** $TV(AB, BA)$ vs. micro-steps k for CIFAR-100/ViT-B/16/resonant strong. Left: *no break*. Right: *break*.

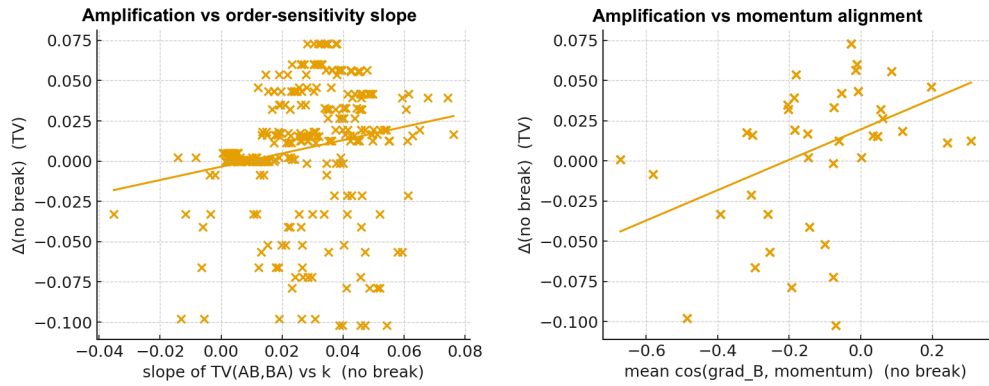


Figure 5: **Amplification vs. order sensitivity (left).** Configurations with a steeper $TV(AB, BA)$ slope (no break) exhibit larger Δ . **Amplification vs. momentum alignment (right).** Each point corresponds to a configuration. Greater pre- B alignment predicts larger Δ . Least-squares fits are shown.

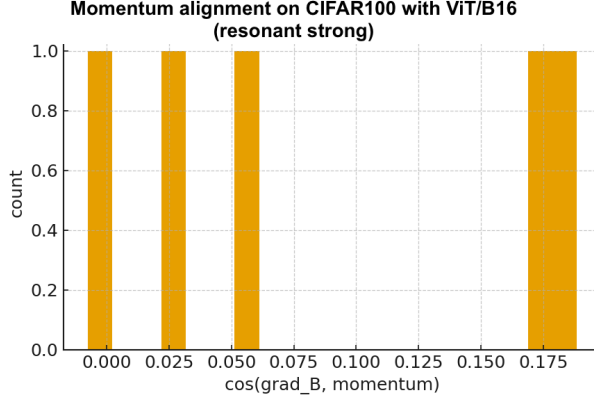


Figure 6: **Momentum alignment (no break).** Histogram of $\cos(\nabla_B, m)$; mass > 0 indicates optimizer carryover aligns with the upcoming B update.

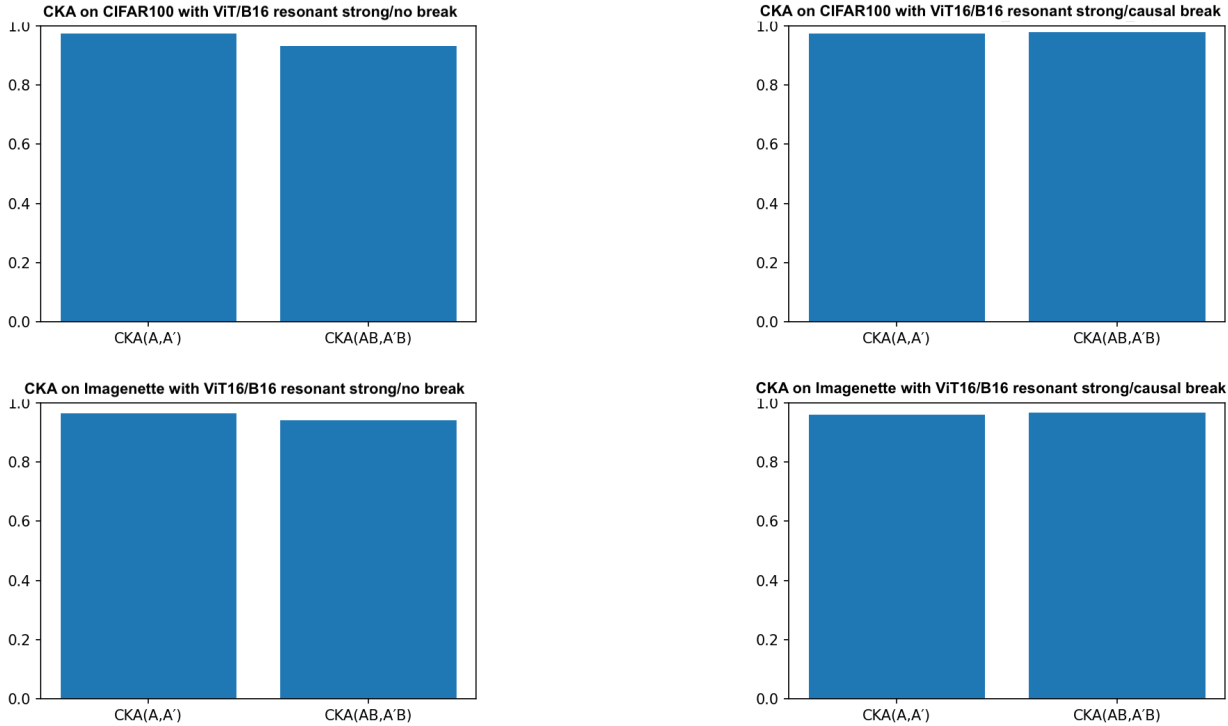


Figure 7: **Penultimate-layer CKA.** Left: *no break*. Right: *break*. Top: CIFAR-100. Bottom: Imagenette. Break increases $\text{CKA}(AB, A'B)$ relative to $\text{CKA}(A, A')$.

For the setups in Fig. 4, the non-commute curve $\text{TV}(AB, BA)$ increases with the number of micro-steps k , evidencing order sensitivity even at short horizons. The slope is typically steeper without a break and flattens with a break, consistent with optimizer carryover as a driver of non-commutativity. Configurations whose non-commute curve grows faster with micro-step depth also exhibit larger Δ . The slope of $\text{TV}(AB, BA)$ vs. k (no break) correlates with Δ : Pearson $r = 0.184$ ($p = 1.38 \times 10^{-3}$) and Spearman $\rho = 0.329$ ($p = 5.45 \times 10^{-9}$) across configurations (Fig. 5 (left)). This links the back-flow witness to order-dependence.

We directly log the cosine between the B -gradient and the momentum buffer just before the first B step. Without a break, the distribution concentrates above zero (Fig. 6), diagnosing *alignment* that explains amplification ($\Delta_{BF} > 0$). With a break, alignment vanishes by construction and Δ_{BF} attenuates or flips. Beyond the qualitative histogram, Δ scales with pre- B momentum alignment: across configurations (dataset \times model \times regime; no-break), we find Pearson $r = 0.409$ (p

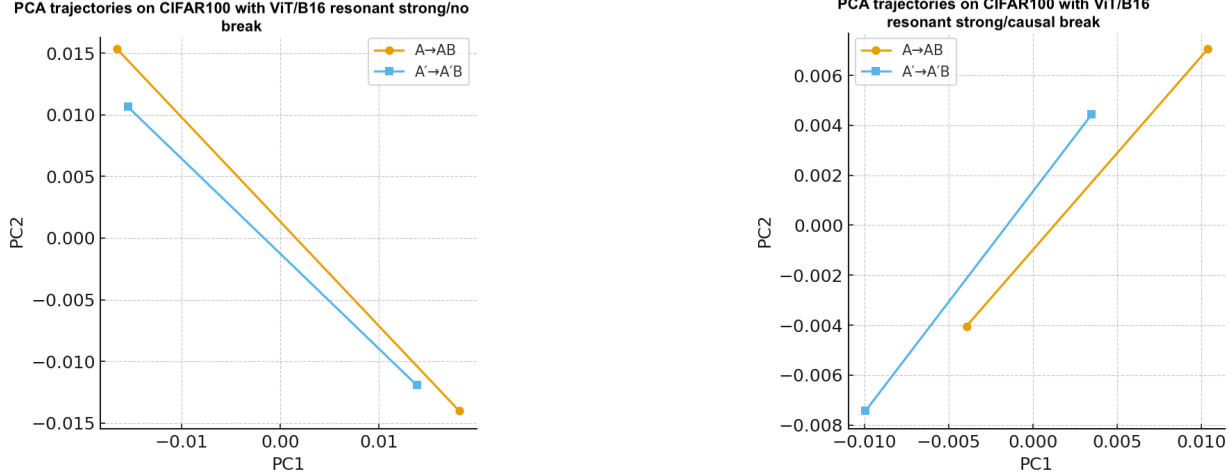


Figure 8: **Function-space trajectories.** Displacements and branch separation are larger without a break (left); a break shortens and aligns paths (right).

$= 4.09 \times 10^{-11}$) and Spearman $\rho = 0.454$ ($p = 1.37 \times 10^{-13}$) between Δ and the mean $\cos(\nabla_B, m)$ (Fig. 5 (right)). This dose–response matches the linearized prediction in §3.5. After a causal break, alignment is null by construction and the amplification collapses. To probe feature-space consequences, we compare penultimate-layer linear CKA for (A, A') vs. $(AB, A'B)$. Under a break, $\text{CKA}(AB, A'B)$ typically exceeds $\text{CKA}(A, A')$ (realignment/attenuation); without a break, the ordering often reverses (divergence/amplification), cf. Fig. 7. Function-space PCA trajectories show the same pattern: longer $A \rightarrow AB$ displacements and wider branch separation without a break; convergence or crossing with a break (Fig. 8).

The negative regime behaves as a control: means $\approx (5\text{--}6) \times 10^{-4}$ and medians $\approx 10^{-7}$ under both conditions. We observe multiple narrow-CI cases (95% CI half-width $\leq 2 \times 10^{-4}$ in nine per condition), supporting the stability of the estimates. TOST with margin $\varepsilon = 10^{-3}$ classifies many break-condition effects as practically null, while rejecting nullity for no-break amplification; see Appendix for per-setup statistics.

As a falsification check, placebo runs with $A = A'$ (identical augmentations) yield Δ statistically indistinguishable from zero (95% CIs spanning 0); likewise, no-break runs with $\mu=0$ collapse to the break baseline, consistent with optimizer buffers mediating back-flow. Regarding the limitations of this work we restrict to short two-step interventions, image classification benchmarks, and standard vision backbones; we study the existence and controllability of memory rather than downstream benefits. Our diagnostic complements, not replaces, SDE/Markov analyses, and it inherits the usual caveats of probe design (choice of B , probe set, metric).

6 Conclusions

The memory we detect is *intentional in mechanism*—optimizer state is carried across steps by design—but *unintended in consequence*: it induces operational non-Markovianity, whereby the effect of a fixed second intervention B depends on the immediate history A . Whether such memory is helpful or harmful depends on the alignment between training order and target generalization. Our witness Δ_{BF} offers a direct diagnostic: it quantifies when optimizer memory amplifies prior updates (as in “resonant” schedules), and when it should be collapsed with a causal break before switching regimes. We identify optimizer state as a *causal driver* of observable back-flow. It systematically amplifies the influence of A on subsequent B , induces order sensitivity ($AB \neq BA$), and can be neutralized by a simple reset of optimizer buffers. This establishes a practical intervention that links mechanism and measurement. The phenomenon is robust: we observe consistent effects across datasets (CIFAR-100, Imagenette), architectures (SmallCNN, ResNet-18, VGG-11, MobileNetV2, ViT-B/16), divergences (TV, JS, H), and training regimes. These results demonstrate that optimizer-induced memory is a pervasive and measurable feature of modern training dynamics, and that back-flow provides a principled, operational handle for studying and controlling it.

References

- [1] Ohad Shamir. Without-replacement sampling for stochastic gradient methods. *Advances in neural information processing systems*, 29, 2016.
- [2] M. Gürbüzbalaban, A. Ozdaglar, and P. A. Parrilo. Why random reshuffling beats stochastic gradient descent. *Mathematical Programming*, 186(1–2):49–84, October 2019.
- [3] Ilya Sutskever, James Martens, George Dahl, and Geoffrey Hinton. On the importance of initialization and momentum in deep learning. In *International conference on machine learning*, pages 1139–1147. pmlr, 2013.
- [4] Gabriel Goh. Why momentum really works. *Distill*, 2(4):e6, 2017.
- [5] Mathieu Even. Stochastic gradient descent under markovian sampling schemes. In *International Conference on Machine Learning*, pages 9412–9439. PMLR, 2023.
- [6] Léon Bottou, Frank E Curtis, and Jorge Nocedal. Optimization methods for large-scale machine learning. *SIAM review*, 60(2):223–311, 2018.
- [7] Stephan Mandt, Matthew D Hoffman, and David M Blei. Stochastic gradient descent as approximate bayesian inference. *Journal of Machine Learning Research*, 18(134):1–35, 2017.
- [8] Heinz-Peter Breuer, Elsi-Mari Laine, and Jyrki Piilo. Measure for the degree of non-markovian behavior of quantum processes in open systems. *Physical review letters*, 103(21):210401, 2009.
- [9] Ángel Rivas, Susana F Huelga, and Martin B Plenio. Quantum non-markovianity: characterization, quantification and detection. *Reports on Progress in Physics*, 77(9):094001, 2014.
- [10] Felix A Pollock, César Rodríguez-Rosario, Thomas Frauenheim, Mauro Paternostro, and Kavan Modi. Non-markovian quantum processes: Complete framework and efficient characterization. *Physical Review A*, 97(1):012127, 2018.
- [11] Felix A Pollock, César Rodríguez-Rosario, Thomas Frauenheim, Mauro Paternostro, and Kavan Modi. Operational markov condition for quantum processes. *Physical review letters*, 120(4):040405, 2018.
- [12] Simon Milz and Kavan Modi. Quantum stochastic processes and quantum non-markovian phenomena. *PRX Quantum*, 2(3):030201, 2021.
- [13] Gregory AL White, Felix A Pollock, Lloyd CL Hollenberg, Kavan Modi, and Charles D Hill. Non-markovian quantum process tomography. *PRX Quantum*, 3(2):020344, 2022.
- [14] Shashank Rajput, Anant Gupta, and Dimitris Papailiopoulos. Closing the convergence gap of sgd without replacement. In *International Conference on Machine Learning*, pages 7964–7973. PMLR, 2020.
- [15] Yurii Nesterov. A method for solving the convex programming problem with convergence rate $o(1/k^2)$. In *Dokl akad nauk Sssr*, volume 269, page 543, 1983.
- [16] Boris T Polyak. Some methods of speeding up the convergence of iteration methods. *Ussr computational mathematics and mathematical physics*, 4(5):1–17, 1964.
- [17] Qianxiao Li, Cheng Tai, et al. Stochastic modified equations and adaptive stochastic gradient algorithms. In *International Conference on Machine Learning*, pages 2101–2110. PMLR, 2017.
- [18] Thinh T Doan, Lam M Nguyen, Nhan H Pham, and Justin Romberg. Finite-time analysis of stochastic gradient descent under markov randomness. *arXiv preprint arXiv:2003.10973*, 2020.
- [19] Ron Dorfman and Kfir Yehuda Levy. Adapting to mixing time in stochastic optimization with markovian data. In *International Conference on Machine Learning*, pages 5429–5446. PMLR, 2022.
- [20] Umut Simsekli, Levent Sagun, and Mert Gurbuzbalaban. A tail-index analysis of stochastic gradient noise in deep neural networks. In *International Conference on Machine Learning*, pages 5827–5837. PMLR, 2019.
- [21] Zhanxing Zhu, Jingfeng Wu, Bing Yu, Lei Wu, and Jinwen Ma. The anisotropic noise in stochastic gradient descent: Its behavior of escaping from sharp minima and regularization effects. *arXiv preprint arXiv:1803.00195*, 2018.
- [22] Jiayuan Ye, Anastasia Borovykh, Soufiane Hayou, and Reza Shokri. Leave-one-out distinguishability in machine learning. *arXiv preprint arXiv:2309.17310*, 2023.
- [23] Nicholas Carlini, Chang Liu, Úlfar Erlingsson, Jernej Kos, and Dawn Song. The secret sharer: Evaluating and testing unintended memorization in neural networks. In *28th USENIX security symposium (USENIX security 19)*, pages 267–284, 2019.

- [24] Nicholas Carlini, Florian Tramer, Eric Wallace, Matthew Jagielski, Ariel Herbert-Voss, Katherine Lee, Adam Roberts, Tom Brown, Dawn Song, Ulfar Erlingsson, et al. Extracting training data from large language models. In *30th USENIX security symposium (USENIX Security 21)*, pages 2633–2650, 2021.
- [25] Pang Wei Koh and Percy Liang. Understanding black-box predictions via influence functions. In *International conference on machine learning*, pages 1885–1894. PMLR, 2017.
- [26] Garima Pruthi, Frederick Liu, Satyen Kale, and Mukund Sundararajan. Estimating training data influence by tracing gradient descent. *Advances in Neural Information Processing Systems*, 33:19920–19930, 2020.
- [27] Chih-Kuan Yeh, Joon Kim, Ian En-Hsu Yen, and Pradeep K Ravikumar. Representer point selection for explaining deep neural networks. *Advances in neural information processing systems*, 31, 2018.
- [28] Simon Kornblith, Mohammad Norouzi, Honglak Lee, and Geoffrey Hinton. Similarity of neural network representations revisited. In *International conference on machine learning*, pages 3519–3529. PMLR, 2019.
- [29] MohammadReza Davari, Stefan Horoi, Amine Natik, Guillaume Lajoie, Guy Wolf, and Eugene Belilovsky. Reliability of cka as a similarity measure in deep learning. *arXiv preprint arXiv:2210.16156*, 2022.

A PROOFS

Proposition 3.1 Let \mathcal{Z} be a (standard Borel) observation space for the probe observable, and let $\mathcal{P}(\mathcal{Z})$ denote the set of probability measures on \mathcal{Z} . Fix a family of first-step instruments \mathcal{I} and a common second-step instrument B . For each $I \in \mathcal{I}$, let $P_I \in \mathcal{P}(\mathcal{Z})$ be the (pre- B) predictive distribution on the probe, and let $Q_I \in \mathcal{P}(\mathcal{Z})$ be the (post- B) predictive distribution. Assume the two-time process is *operationally Markov at the observable for B* , namely: there exists a Markov kernel (classical channel) $\Lambda_B : \mathcal{P}(\mathcal{Z}) \rightarrow \mathcal{P}(\mathcal{Z})$ such that

$$Q_I = \Lambda_B(P_I) \quad \text{for all } I \in \mathcal{I}.$$

Let $D : \mathcal{P}(\mathcal{Z}) \times \mathcal{P}(\mathcal{Z}) \rightarrow [0, \infty]$ be any divergence that is *contractive under classical channels*, i.e., $D(\Lambda p, \Lambda q) \leq D(p, q)$ for all probability measures p, q and Markov kernels Λ . Define the back-flow of distinguishability for any pair $I, I' \in \mathcal{I}$ by

$$\Delta^{(I,B)}(I, I') := D(Q_I, Q_{I'}) - D(P_I, P_{I'}) .$$

Then $\Delta^{(I,B)}(I, I') \leq 0$ for all $I, I' \in \mathcal{I}$.

Proof By operational Markovianity at the observable for B , there exists a *fixed* Markov kernel Λ_B such that $Q_I = \Lambda_B(P_I)$ and $Q_{I'} = \Lambda_B(P_{I'})$ for all instruments I, I' . By contractivity of D under classical channels (data-processing inequality),

$$D(Q_I, Q_{I'}) = D(\Lambda_B(P_I), \Lambda_B(P_{I'})) \leq D(P_I, P_{I'}) .$$

Rearranging gives $D(Q_I, Q_{I'}) - D(P_I, P_{I'}) \leq 0$, i.e., $\Delta^{(I,B)}(I, I') \leq 0$. Since I, I' were arbitrary, the claim holds for all pairs.

Remarks. (i) In the discrete case, Λ_B is a stochastic matrix acting on probability vectors, and the proof reduces to $D(\Lambda_B p, \Lambda_B q) \leq D(p, q)$. (ii) The assumption on D holds for standard contractive divergences (e.g., total variation, Hellinger, Jensen–Shannon, and more generally Csiszár f -divergences under mild regularity). (iii) Equality $\Delta^{(I,B)} = 0$ occurs, e.g., when Λ_B is *sufficient* for the pair $(P_I, P_{I'})$ in the sense that it preserves their statistical distance as measured by D .

A.1 Proof of Proposition 3.2

Proposition 3.2 Let D be any divergence on probability measures that satisfies data processing: $D(\Lambda p, \Lambda q) \leq D(p, q)$ for all Markov kernels Λ and all p, q . Assume the operational Markov condition (4) for the second-step observable B , i.e., there exists a (fixed) classical channel Λ_B such that

$$\Phi_2^{(I,B)} = \Lambda_B \Phi_1^{(I)} \quad \text{for every first-step instrument } I. \tag{8}$$

For any two first-step instruments A, A' , define the back-flow of distinguishability

$$\Delta^{(I,B)} := D(\Phi_2^{(A,B)}, \Phi_2^{(A',B)}) - D(\Phi_1^{(A)}, \Phi_1^{(A')}).$$

Then $\Delta^{(I,B)} \leq 0$.

Proof Fix any two first-step instruments A, A' . Set $P = \Phi_1^{(A)}$ and $Q = \Phi_1^{(A')}$. By (8),

$$\Phi_2^{(A,B)} = \Lambda_B P \quad \text{and} \quad \Phi_2^{(A',B)} = \Lambda_B Q.$$

Applying data processing for D with the channel Λ_B yields

$$D(\Phi_2^{(A,B)}, \Phi_2^{(A',B)}) = D(\Lambda_B P, \Lambda_B Q) \leq D(P, Q) = D(\Phi_1^{(A)}, \Phi_1^{(A')}).$$

Rearranging gives $\Delta^{(I,B)} \leq 0$, as claimed.

Remarks. (1) The argument is agnostic to the sample space (finite or general Borel) and to the particular choice of D , provided D obeys data processing (e.g., total variation, Hellinger, Jensen–Shannon, and Csiszár f -divergences under standard regularity). (2) If you use the metric \sqrt{JS} , data processing holds and the same conclusion follows verbatim. (3) If you later introduce an *approximate* OMC, $\|\Phi_2^{(I,B)} - \Lambda_B \Phi_1^{(I)}\|_D \leq \eta_I$ for all I and a triangle-inequality divergence $\|\cdot\|_D$, then

$$\Delta^{(I,B)} \leq \eta_A + \eta_{A'},$$

by a two-sided triangle inequality combined with contractivity of D ; this yields a stable, quantitative relaxation of Proposition 3.2.

Proof of Theorem 3.4 Let \mathcal{Q}, \mathcal{O} be standard Borel spaces. Let $\mathcal{O} : \mathcal{Q} \rightsquigarrow \mathcal{O}$ be the probe observable (a Markov kernel) and let $\mathcal{K}_B : \mathcal{Q} \rightsquigarrow \mathcal{Q}$ be the second-step dynamics for instrument B . For a first-step instrument I , write $\pi_1^{(I)} \in \mathcal{P}(\mathcal{Q})$ for the latent state after step 1 and $\Phi_1^{(I)} := \pi_1^{(I)} \mathcal{O} \in \mathcal{P}(\mathcal{O})$ for the corresponding predictive (pre- B) observable law. Assume:

(Break) *Causal break* \mathcal{B} is applied between step 1 and B , so that the post-break latent state depends on I only via $\Phi_1^{(I)}$, i.e., there exists a Markov kernel $\mathcal{R} : \mathcal{O} \rightsquigarrow \mathcal{Q}$ with

$$\tilde{\pi}_1^{(I)} = \Phi_1^{(I)} \mathcal{R} \quad \text{for all } I.$$

(Suff) *Sufficiency of \mathcal{O} for B on \mathcal{Q}* : there exists a Markov kernel $\Lambda_B : \mathcal{O} \rightsquigarrow \mathcal{O}$ such that

$$\mu \mathcal{R} \mathcal{K}_B \mathcal{O} = \mu \Lambda_B \quad \text{for all } \mu \in \mathcal{P}(\mathcal{O}). \quad (9)$$

(Equivalently, for all $\pi \in \mathcal{P}(\mathcal{Q})$ one has $\pi \mathcal{K}_B \mathcal{O} = (\pi \mathcal{O}) \Lambda_B$.)

Then for all first-step instruments I ,

$$\Phi_2^{(I,B)} = \Lambda_B [\Phi_1^{(I)}].$$

Consequently, for any divergence D that is contractive under classical channels (data processing), the back-flow satisfies $\Delta^{(I,B)} \leq 0$.

Proof By the causal break, the latent state just before applying B is $\tilde{\pi}_1^{(I)} = \Phi_1^{(I)} \mathcal{R}$. Pushing it forward through B and then observing via \mathcal{O} gives

$$\Phi_2^{(I,B)} = \tilde{\pi}_1^{(I)} \mathcal{K}_B \mathcal{O} = (\Phi_1^{(I)} \mathcal{R}) \mathcal{K}_B \mathcal{O} = \Phi_1^{(I)} (\mathcal{R} \mathcal{K}_B \mathcal{O}).$$

By sufficiency (9), the composite $\mathcal{R} \mathcal{K}_B \mathcal{O}$ factors through a *fixed* observable channel $\Lambda_B : \mathcal{O} \rightsquigarrow \mathcal{O}$ independent of I , hence

$$\Phi_2^{(I,B)} = \Phi_1^{(I)} \Lambda_B = \Lambda_B [\Phi_1^{(I)}].$$

This proves the first claim.

For the back-flow bound, let A, A' be any two first-step instruments and set $P = \Phi_1^{(A)}, Q = \Phi_1^{(A')}$. Then

$$\Phi_2^{(A,B)} = \Lambda_B P, \quad \Phi_2^{(A',B)} = \Lambda_B Q.$$

By data processing (contractivity) of D under classical channels,

$$D(\Phi_2^{(A,B)}, \Phi_2^{(A',B)}) = D(\Lambda_B P, \Lambda_B Q) \leq D(P, Q) = D(\Phi_1^{(A)}, \Phi_1^{(A')}).$$

Rearranging yields $\Delta^{(I,B)} \leq 0$.

Notes on assumptions.

- The *causal break* is encoded by $\mathcal{R} : \mathcal{O} \rightsquigarrow \mathcal{Q}$; it re-prepares the latent state using only the observed law from step 1, thus erasing any dependence on the pre-history beyond $\Phi_1^{(I)}$.
- The *sufficiency* condition is the standard Blackwell–Sherman–Stein notion: the pair $(\mathcal{K}_B, \mathcal{O})$ *garbles* through the statistic \mathcal{O} , i.e. there exists a channel Λ_B on observables such that for all priors π on \mathcal{Q} , $(\pi\mathcal{O})\Lambda_B = \pi\mathcal{K}_B\mathcal{O}$. This yields (9) globally on $\mathcal{P}(\mathcal{O})$ (no extension argument is needed).
- In discrete settings, $\mathcal{R}, \mathcal{K}_B, \mathcal{O}, \Lambda_B$ are stochastic matrices and the proof reduces to associativity of matrix multiplication.

B ADDITIONAL TABLESTable 3: **Per-group significance by metric.** A checkmark means the 95% CI for Δ excludes 0. Break: no vs br.

Dataset	Model	Regime	Stage	Break	TV	JS	Hell
cifar100	mobilenetv2	negative	early	br	✓	✓	✓
cifar100	mobilenetv2	negative	early	no	✓	✓	✓
cifar100	mobilenetv2	orthogonal	early	br	✓	✓	✓
cifar100	mobilenetv2	orthogonal	early	no	✓	✓	✓
cifar100	mobilenetv2	resonant mid	early	br	✓	✓	✓
cifar100	mobilenetv2	resonant mid	early	no	✓	✓	✓
cifar100	mobilenetv2	resonant strong	early	br	✓	✓	✓
cifar100	mobilenetv2	resonant strong	early	no	✓	✓	✓
cifar100	mobilenetv2	standard	early	br	✓	✓	✓
cifar100	mobilenetv2	standard	early	no	✓	✓	✓
cifar100	resnet18	negative	early	br	✓	✓	✓
cifar100	resnet18	negative	early	no	✓	✓	✓
cifar100	resnet18	orthogonal	early	br	✓	✓	✓
cifar100	resnet18	orthogonal	early	no	✓	✓	✓
cifar100	resnet18	resonant mid	early	br	✓	✓	✓
cifar100	resnet18	resonant mid	early	no	✓	✓	✓
cifar100	resnet18	resonant strong	early	br	✓	✓	✓
cifar100	resnet18	resonant strong	early	no	✓	✓	✓
cifar100	resnet18	standard	early	br	—	✓	—
cifar100	resnet18	standard	early	no	✓	✓	✓
cifar100	smallcnn	negative	early	br	✓	—	✓
cifar100	smallcnn	negative	early	no	✓	—	✓
cifar100	smallcnn	orthogonal	early	br	—	—	—
cifar100	smallcnn	orthogonal	early	no	✓	✓	✓
cifar100	smallcnn	resonant mid	early	br	✓	✓	✓
cifar100	smallcnn	resonant mid	early	no	✓	✓	✓
cifar100	smallcnn	resonant strong	early	br	✓	✓	✓
cifar100	smallcnn	resonant strong	early	no	✓	✓	✓
cifar100	smallcnn	standard	early	br	✓	✓	✓
cifar100	smallcnn	standard	early	no	✓	✓	✓
cifar100	vgg11	negative	early	br	✓	✓	✓
cifar100	vgg11	negative	early	no	✓	—	✓
cifar100	vgg11	orthogonal	early	br	✓	✓	✓
cifar100	vgg11	orthogonal	early	no	✓	✓	✓
cifar100	vgg11	resonant mid	early	br	✓	✓	✓
cifar100	vgg11	resonant mid	early	no	—	—	—
cifar100	vgg11	resonant strong	early	br	✓	✓	✓
cifar100	vgg11	resonant strong	early	no	✓	✓	✓
cifar100	vgg11	standard	early	br	✓	✓	✓
cifar100	vgg11	standard	early	no	✓	✓	✓

continued on next page

Dataset	Model	Regime	Stage	Break	TV	JS	Hell
cifar100	vit-b-16	negative	early	br	✓	—	✓
cifar100	vit-b-16	negative	early	no	✓	—	✓
cifar100	vit-b-16	orthogonal	early	br	✓	✓	✓
cifar100	vit-b-16	orthogonal	early	no	✓	✓	✓
cifar100	vit-b-16	resonant mid	early	br	✓	✓	✓
cifar100	vit-b-16	resonant mid	early	no	✓	✓	✓
cifar100	vit-b-16	resonant strong	early	br	✓	✓	✓
cifar100	vit-b-16	resonant strong	early	no	✓	✓	✓
cifar100	vit-b-16	standard	early	br	✓	✓	✓
cifar100	vit-b-16	standard	early	no	✓	✓	✓
imagenette	mobilenetv2	negative	early	br	✓	✓	✓
imagenette	mobilenetv2	negative	early	no	✓	✓	✓
imagenette	mobilenetv2	orthogonal	early	br	✓	✓	✓
imagenette	mobilenetv2	orthogonal	early	no	✓	✓	✓
imagenette	mobilenetv2	resonant mid	early	br	✓	✓	✓
imagenette	mobilenetv2	resonant mid	early	no	✓	✓	✓
imagenette	mobilenetv2	resonant strong	early	br	✓	✓	✓
imagenette	mobilenetv2	resonant strong	early	no	✓	✓	✓
imagenette	mobilenetv2	standard	early	br	✓	✓	✓
imagenette	mobilenetv2	standard	early	no	✓	✓	✓
imagenette	resnet18	negative	early	br	✓	—	✓
imagenette	resnet18	negative	early	no	✓	—	✓
imagenette	resnet18	orthogonal	early	br	✓	✓	✓
imagenette	resnet18	orthogonal	early	no	✓	✓	✓
imagenette	resnet18	resonant mid	early	br	✓	✓	✓
imagenette	resnet18	resonant mid	early	no	✓	✓	✓
imagenette	resnet18	resonant strong	early	br	✓	✓	✓
imagenette	resnet18	resonant strong	early	no	✓	✓	✓
imagenette	resnet18	standard	early	br	✓	✓	✓
imagenette	resnet18	standard	early	no	✓	✓	✓
imagenette	smallcnn	negative	early	br	✓	—	✓
imagenette	smallcnn	negative	early	no	✓	—	✓
imagenette	smallcnn	orthogonal	early	br	✓	✓	✓
imagenette	smallcnn	orthogonal	early	no	—	—	—
imagenette	smallcnn	resonant mid	early	br	✓	✓	✓
imagenette	smallcnn	resonant mid	early	no	✓	✓	✓
imagenette	smallcnn	resonant strong	early	br	✓	✓	✓
imagenette	smallcnn	resonant strong	early	no	✓	✓	✓
imagenette	smallcnn	standard	early	br	✓	✓	✓
imagenette	smallcnn	standard	early	no	—	—	—
imagenette	vgg11	negative	early	br	✓	—	✓
imagenette	vgg11	negative	early	no	✓	—	✓
imagenette	vgg11	orthogonal	early	br	✓	✓	✓
imagenette	vgg11	orthogonal	early	no	✓	✓	✓
imagenette	vgg11	resonant mid	early	br	—	✓	—
imagenette	vgg11	resonant mid	early	no	✓	✓	✓
imagenette	vgg11	resonant strong	early	br	✓	✓	✓
imagenette	vgg11	resonant strong	early	no	✓	✓	✓
imagenette	vgg11	standard	early	br	✓	✓	✓
imagenette	vgg11	standard	early	no	✓	✓	✓
imagenette	vit-b-16	negative	early	br	✓	—	✓
imagenette	vit-b-16	negative	early	no	✓	—	✓
imagenette	vit-b-16	orthogonal	early	br	✓	—	✓
imagenette	vit-b-16	orthogonal	early	no	✓	✓	✓
imagenette	vit-b-16	resonant mid	early	br	✓	✓	—

continued on next page

Dataset	Model	Regime	Stage	Break	TV	JS	Hell
imagenette	vit-b-16	resonant mid	early	no	✓	✓	✓
imagenette	vit-b-16	resonant strong	early	br	✓	✓	✓
imagenette	vit-b-16	resonant strong	early	no	✓	✓	✓
imagenette	vit-b-16	standard	early	br	✓	✓	✓
imagenette	vit-b-16	standard	early	no	✓	✓	✓

Table 4: **Metric agreement summary.** Counts over all {dataset, model, regime, stage, break} groups.

Total groups	100
TV significant	97
JS significant	82
Hellinger significant	94
TV \wedge Hellinger significant	93 / 100
TV \wedge JS significant	80 / 100
All three significant	80 / 100
TV-only significant	0 / 100
non-TV-only significant	2 / 100
None significant	4 / 100

For each {dataset, model, regime, stage, break} configuration we report the mean $\bar{\Delta}$, a nonparametric 95% bootstrap CI, the number of repeats n (pooled across seeds), the CI half-width, and TOST results for $\varepsilon = 10^{-3}$; see Table 6. A compact control summary for the **negative regime** (means and medians under both optimizer conditions) appears in Table 5.

Break	Mean $\bar{\Delta}$	Median $\bar{\Delta}$	Count
no	0.000597	0.000000	10
br	0.000516	0.000000	10

Table 5: **Negative regime as control (TV).** Means and medians across setups under no-break and break conditions.

We complement bootstrap CIs with Benjamini–Hochberg (BH) false-discovery-rate control applied to two-sided tests of $H_0 : \mathbb{E}[\Delta] = 0$ per configuration. At FDR 5%, TV: 94/100, Hellinger: 93/100, and JS: 81/100 groups remain significant; conclusions are unchanged. Per-setup tables report raw p and BH q -values alongside 95% bootstrap CIs.

Table 6: **Per-setup statistics with FDR (TV).** Mean $\bar{\Delta}$, 95% bootstrap CI, n , raw two-sided p , and BH-FDR q -value across the 100 TV tests.

Dataset	Model	Regime	Stage	Break	$\bar{\Delta}$	95% CI	n	p (two-sided)	q (BH)
cifar100	mobilenetv2	negative	early	no	0.000805	[0.000750, 0.000858]	672	0.00e+00	0.00e+00
cifar100	mobilenetv2	negative	early	br	0.000887	[0.000799, 0.000974]	352	0.00e+00	0.00e+00
cifar100	mobilenetv2	orthogonal	early	no	0.019348	[0.017077, 0.021519]	1280	0.00e+00	0.00e+00
cifar100	mobilenetv2	orthogonal	early	br	-0.051217	[-0.054100, -0.048418]	896	0.00e+00	0.00e+00
cifar100	mobilenetv2	resonant mid	early	no	0.012552	[0.010594, 0.014415]	1280	0.00e+00	0.00e+00
cifar100	mobilenetv2	resonant mid	early	br	-0.047301	[-0.049171, -0.045360]	1280	0.00e+00	0.00e+00
cifar100	mobilenetv2	resonant strong	early	no	0.041931	[0.039873, 0.044059]	1280	0.00e+00	0.00e+00
cifar100	mobilenetv2	resonant strong	early	br	-0.027104	[-0.029174, -0.025083]	1280	0.00e+00	0.00e+00
cifar100	mobilenetv2	standard	early	no	0.015456	[0.014300, 0.016628]	1280	0.00e+00	0.00e+00
cifar100	mobilenetv2	standard	early	br	-0.036990	[-0.038282, -0.035757]	1280	0.00e+00	0.00e+00
cifar100	resnet18	negative	early	no	0.000002	[0.000002, 0.000003]	320	0.00e+00	0.00e+00
cifar100	resnet18	negative	early	br	0.000002	[0.000002, 0.000003]	320	0.00e+00	0.00e+00
cifar100	resnet18	orthogonal	early	no	-0.041033	[-0.049857, -0.032092]	640	0.00e+00	0.00e+00
cifar100	resnet18	orthogonal	early	br	-0.025690	[-0.034570, -0.016585]	640	8.42e-08	9.91e-08
cifar100	resnet18	resonant mid	early	no	-0.102151	[-0.109609, -0.094925]	640	0.00e+00	0.00e+00
cifar100	resnet18	resonant mid	early	br	-0.109642	[-0.117547, -0.102230]	640	0.00e+00	0.00e+00
cifar100	resnet18	resonant strong	early	no	-0.078765	[-0.086192, -0.071730]	640	0.00e+00	0.00e+00
cifar100	resnet18	resonant strong	early	br	-0.090973	[-0.098795, -0.083216]	640	0.00e+00	0.00e+00
cifar100	resnet18	standard	early	no	0.015820	[0.012206, 0.019341]	640	0.00e+00	0.00e+00
cifar100	resnet18	standard	early	br	0.004149	[-0.000556, 0.008643]	640	8.12e-02	8.45e-02
cifar100	smallcnn	negative	early	no	0.000000	[0.000000, 0.000000]	320	1.30e-07	1.52e-07
cifar100	smallcnn	negative	early	br	0.000000	[0.000000, 0.000000]	320	5.35e-14	6.86e-14
cifar100	smallcnn	orthogonal	early	no	0.032157	[0.020628, 0.043640]	640	4.04e-08	4.81e-08
cifar100	smallcnn	orthogonal	early	br	0.011148	[-0.000787, 0.022086]	640	6.42e-02	6.76e-02
cifar100	smallcnn	resonant mid	early	no	-0.072155	[-0.080590, -0.063648]	640	0.00e+00	0.00e+00
cifar100	smallcnn	resonant mid	early	br	-0.055786	[-0.065107, -0.046302]	640	0.00e+00	0.00e+00
cifar100	smallcnn	resonant strong	early	no	-0.051914	[-0.062084, -0.041965]	640	0.00e+00	0.00e+00
cifar100	smallcnn	resonant strong	early	br	-0.039207	[-0.048721, -0.029565]	640	1.40e-14	1.82e-14
cifar100	smallcnn	standard	early	no	-0.008411	[-0.011692, -0.004860]	640	2.89e-06	3.25e-06
cifar100	smallcnn	standard	early	br	0.009618	[0.006112, 0.013103]	640	1.98e-07	2.27e-07
cifar100	vgg11	negative	early	no	0.000000	[0.000000, 0.000000]	320	7.86e-13	9.71e-13
cifar100	vgg11	negative	early	br	0.000000	[0.000000, 0.000000]	320	9.08e-05	9.98e-05
cifar100	vgg11	orthogonal	early	no	-0.021196	[-0.023877, -0.018546]	640	0.00e+00	0.00e+00
cifar100	vgg11	orthogonal	early	br	-0.067943	[-0.070836, -0.065066]	640	0.00e+00	0.00e+00
cifar100	vgg11	resonant mid	early	no	-0.001379	[-0.003891, 0.000891]	640	2.56e-01	2.64e-01
cifar100	vgg11	resonant mid	early	br	-0.066817	[-0.068861, -0.064791]	640	0.00e+00	0.00e+00
cifar100	vgg11	resonant strong	early	no	0.033132	[0.030105, 0.035919]	640	0.00e+00	0.00e+00

continued on next page

Dataset	Model	Regime	Stage	Break	$\bar{\Delta}$	95% CI	n	p (two-sided)	q (BH)
cifar100	vgg11	resonant strong	early	br	-0.049203	[-0.051429, -0.046999]	640	0.00e+00	0.00e+00
cifar100	vgg11	standard	early	no	0.011491	[0.010437, 0.012573]	640	0.00e+00	0.00e+00
cifar100	vgg11	standard	early	br	-0.029600	[-0.030528, -0.028720]	640	0.00e+00	0.00e+00
cifar100	vit_b16	negative	early	no	0.000000	[0.000000, 0.000000]	320	0.00e+00	0.00e+00
cifar100	vit_b16	negative	early	br	0.000000	[0.000000, 0.000000]	320	0.00e+00	0.00e+00
cifar100	vit_b16	orthogonal	early	no	0.016780	[0.015028, 0.018559]	640	0.00e+00	0.00e+00
cifar100	vit_b16	orthogonal	early	br	-0.062900	[-0.064360, -0.061424]	640	0.00e+00	0.00e+00
cifar100	vit_b16	resonant mid	early	no	0.026613	[0.025079, 0.028070]	640	0.00e+00	0.00e+00
cifar100	vit_b16	resonant mid	early	br	-0.044202	[-0.045560, -0.042761]	640	0.00e+00	0.00e+00
cifar100	vit_b16	resonant strong	early	no	0.055668	[0.053859, 0.057515]	640	0.00e+00	0.00e+00
cifar100	vit_b16	resonant strong	early	br	-0.029075	[-0.030643, -0.027431]	640	0.00e+00	0.00e+00
cifar100	vit_b16	standard	early	no	0.012572	[0.011751, 0.013416]	640	0.00e+00	0.00e+00
cifar100	vit_b16	standard	early	br	-0.019568	[-0.020261, -0.018862]	640	0.00e+00	0.00e+00
imagenette	mobilenetv2	negative	early	no	0.005157	[0.004957, 0.005360]	1280	0.00e+00	0.00e+00
imagenette	mobilenetv2	negative	early	br	0.004266	[0.004041, 0.004503]	640	0.00e+00	0.00e+00
imagenette	mobilenetv2	orthogonal	early	no	0.056586	[0.055054, 0.058130]	1280	0.00e+00	0.00e+00
imagenette	mobilenetv2	orthogonal	early	br	0.007169	[0.005253, 0.009030]	640	5.86e-13	7.33e-13
imagenette	mobilenetv2	resonant mid	early	no	0.060175	[0.058912, 0.061466]	1280	0.00e+00	0.00e+00
imagenette	mobilenetv2	resonant mid	early	br	0.015760	[0.014301, 0.017103]	1024	0.00e+00	0.00e+00
imagenette	mobilenetv2	resonant strong	early	no	0.072772	[0.071373, 0.074186]	1280	0.00e+00	0.00e+00
imagenette	mobilenetv2	resonant strong	early	br	0.018428	[0.017107, 0.019800]	1280	0.00e+00	0.00e+00
imagenette	mobilenetv2	standard	early	no	0.043493	[0.042607, 0.044306]	1280	0.00e+00	0.00e+00
imagenette	mobilenetv2	standard	early	br	0.012223	[0.011316, 0.013138]	1280	0.00e+00	0.00e+00
imagenette	resnet18	negative	early	no	0.000003	[0.000003, 0.000004]	320	0.00e+00	0.00e+00
imagenette	resnet18	negative	early	br	0.000003	[0.000003, 0.000004]	320	0.00e+00	0.00e+00
imagenette	resnet18	orthogonal	early	no	-0.033066	[-0.040169, -0.025908]	640	0.00e+00	0.00e+00
imagenette	resnet18	orthogonal	early	br	-0.040914	[-0.049604, -0.032405]	640	0.00e+00	0.00e+00
imagenette	resnet18	resonant mid	early	no	-0.097785	[-0.104683, -0.090893]	640	0.00e+00	0.00e+00
imagenette	resnet18	resonant mid	early	br	-0.091842	[-0.099027, -0.084716]	640	0.00e+00	0.00e+00
imagenette	resnet18	resonant strong	early	no	-0.066178	[-0.072768, -0.059103]	640	0.00e+00	0.00e+00
imagenette	resnet18	resonant strong	early	br	-0.087421	[-0.095146, -0.079758]	640	0.00e+00	0.00e+00
imagenette	resnet18	standard	early	no	0.016140	[0.011878, 0.020230]	640	3.02e-13	3.82e-13
imagenette	resnet18	standard	early	br	-0.022495	[-0.027069, -0.018019]	640	0.00e+00	0.00e+00
imagenette	smallcnn	negative	early	no	0.000000	[0.000000, 0.000000]	320	0.00e+00	0.00e+00
imagenette	smallcnn	negative	early	br	0.000000	[0.000000, 0.000000]	320	0.00e+00	0.00e+00
imagenette	smallcnn	orthogonal	early	no	0.002243	[-0.006734, 0.011739]	640	6.22e-01	6.22e-01
imagenette	smallcnn	orthogonal	early	br	0.011140	[0.002560, 0.020306]	640	1.42e-02	1.54e-02
imagenette	smallcnn	resonant mid	early	no	-0.056493	[-0.063667, -0.049287]	640	0.00e+00	0.00e+00
imagenette	smallcnn	resonant mid	early	br	-0.053091	[-0.060871, -0.044799]	640	0.00e+00	0.00e+00

continued on next page

Dataset	Model	Regime	Stage	Break	$\bar{\Delta}$	95% CI	n	p (two-sided)	q (BH)
imagenette	smallcnn	resonant strong	early	no	-0.032882	[-0.040282, -0.025792]	640	0.00e+00	0.00e+00
imagenette	smallcnn	resonant strong	early	br	-0.040571	[-0.048600, -0.032944]	640	0.00e+00	0.00e+00
imagenette	smallcnn	standard	early	no	0.001042	[-0.001016, 0.003169]	640	3.49e-01	3.55e-01
imagenette	smallcnn	standard	early	br	0.009399	[0.006702, 0.012158]	640	2.92e-11	3.57e-11
imagenette	vgg11	negative	early	no	0.000000	[0.000000, 0.000000]	320	1.34e-06	1.52e-06
imagenette	vgg11	negative	early	br	0.000000	[0.000000, 0.000000]	320	1.28e-08	1.54e-08
imagenette	vgg11	orthogonal	early	no	0.032065	[0.028080, 0.035953]	640	0.00e+00	0.00e+00
imagenette	vgg11	orthogonal	early	br	0.015976	[0.012318, 0.019872]	640	4.44e-16	5.84e-16
imagenette	vgg11	resonant mid	early	no	0.018407	[0.015339, 0.021351]	640	0.00e+00	0.00e+00
imagenette	vgg11	resonant mid	early	br	0.001541	[-0.001617, 0.004896]	640	3.51e-01	3.55e-01
imagenette	vgg11	resonant strong	early	no	0.045932	[0.042310, 0.049204]	640	0.00e+00	0.00e+00
imagenette	vgg11	resonant strong	early	br	0.020064	[0.016778, 0.023461]	640	0.00e+00	0.00e+00
imagenette	vgg11	standard	early	no	0.002099	[0.001116, 0.003087]	640	4.08e-05	4.54e-05
imagenette	vgg11	standard	early	br	-0.005895	[-0.006964, -0.004909]	640	0.00e+00	0.00e+00
imagenette	vit_b16	negative	early	no	0.000000	[0.000000, 0.000000]	320	0.00e+00	0.00e+00
imagenette	vit_b16	negative	early	br	0.000000	[0.000000, 0.000000]	320	0.00e+00	0.00e+00
imagenette	vit_b16	orthogonal	early	no	0.039317	[0.036467, 0.042267]	640	0.00e+00	0.00e+00
imagenette	vit_b16	orthogonal	early	br	-0.003246	[-0.006069, -0.000244]	640	2.97e-02	3.19e-02
imagenette	vit_b16	resonant mid	early	no	0.035099	[0.032329, 0.037743]	640	0.00e+00	0.00e+00
imagenette	vit_b16	resonant mid	early	br	0.002902	[0.000042, 0.005710]	640	4.13e-02	4.39e-02
imagenette	vit_b16	resonant strong	early	no	0.053741	[0.050745, 0.056677]	640	0.00e+00	0.00e+00
imagenette	vit_b16	resonant strong	early	br	0.015032	[0.012409, 0.017768]	640	0.00e+00	0.00e+00
imagenette	vit_b16	standard	early	no	0.017612	[0.016491, 0.018653]	640	0.00e+00	0.00e+00
imagenette	vit_b16	standard	early	br	0.006220	[0.004754, 0.007658]	640	2.22e-16	2.96e-16

C QUANTITATIVE DOSE-RESPONSE (momentum, fixed aug_B).

We model the predicted amplification due to momentum as $A_\mu = \frac{1-\mu^k}{1-\mu}$ and regress the observed back-flow as $\Delta = \alpha + \beta A_\mu + \gamma \rho + \varepsilon$, where ρ is the A - B batch overlap. Using TV under *no break* and configurations with $\text{aug}_B = \text{weak}$ (standard: $k=3, \mu=0.90, \rho=0.5$; resonant_mid: $k=6, \mu=0.95, \rho=0.75$; resonant_strong: $k=6, \mu=0.99, \rho=1.0$), we obtain $n = 30$ dataset \times model points with $R^2 = 0.077$, $\beta = -0.0273$ (0.0184), $p = 1.38 \times 10^{-1}$ and $\gamma = 0.1607$ (0.1235), $p = 1.93 \times 10^{-1}$. Because k and ρ vary across regimes, we also perform a *within-pair* test at fixed $k=6$ (same dataset and model), comparing resonant_strong to resonant_mid: all 10/10 pairs exhibit an increase (strong > mid), with mean lift 0.0251 and 95% CI [0.0208, 0.0288] (paired *t*-test $p = 8.14 \times 10^{-7}$). Numerically, for $k=6$ the amplification factor increases from $A_\mu(\mu=0.95) \approx 5.29$ to $A_\mu(\mu=0.99) \approx 5.90$; the joint increase in A_μ and ρ yields a robust *dose-response* in Δ .

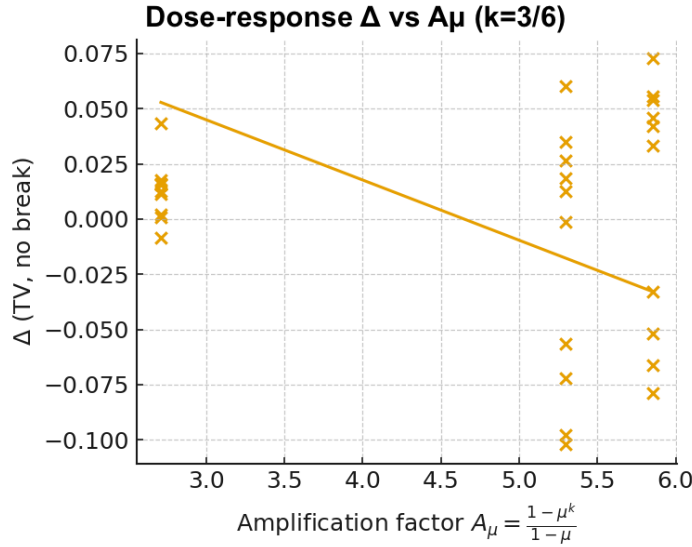


Figure 9: **Dose-response:** TV Δ vs $A_\mu = (1 - \mu^k) / (1 - \mu)$ under *no break* for regimes with $\text{aug}_B = \text{weak}$. Line shows OLS fit at mean overlap. A paired comparison at fixed $k=6$ (not shown) finds strong>mid in 10/10 dataset \times model pairs (mean lift 0.0251, 95% CI [0.0208, 0.0288]).